



# Microfluidic-enhanced 3-D photoanodes with free interfacial energy barrier for photoelectrochemical applications

Zhenao Gu<sup>a,c</sup>, Xiaoqiang An<sup>b</sup>, Huachun Lan<sup>b</sup>, Yu Tian<sup>d</sup>, Jinxing Zhang<sup>d</sup>, Ruiping Liu<sup>a,c,\*</sup>,  
Huijuan Liu<sup>b</sup>, Jiuhui Qu<sup>a,c</sup>

<sup>a</sup> Key Laboratory of Drinking Water Science and Technology, Research Center for Eco-Environmental Sciences, Chinese Academy of Sciences, Beijing 100085, China

<sup>b</sup> Center for Water and Ecology, State Key Joint Laboratory of Environment Simulation and Pollution Control, School of Environment, Tsinghua University, Beijing 100084, China

<sup>c</sup> University of Chinese Academy of Sciences, Beijing 100049, China

<sup>d</sup> Department of Physics, Beijing Normal University, Beijing 100875, China

## ARTICLE INFO

### Keywords:

Flow-through photoanodes  
Internal electrostatic field  
Schottky barrier  
Mass transfer  
Photoelectrochemical

## ABSTRACT

The sluggish reaction kinetics and poor interfacial mass transfer seriously limit the industrial applications of planar photoelectrocatalytic devices. Here, the principle of 3-D flow-through photoanodes with free interfacial barrier for electron transfer and microfluidic channels for reactant transportation was demonstrated. Owing to the epitaxial growth of anisotropic ZnO nanorods with internal electrostatic field onto carbon cloth (CC), the spatial separation of photo-induced charge carriers was realized. Experimental characterizations confirmed the formation of Schottky-barrier-free interface with low electrical resistance for electron transfer, resulting in the significantly decreased onset potential. Compared to traditional planar FTO/ZnO photoanodes, flow-through CC/ZnO photoanodes exhibited 4 times (for Rhodamine B) and 3 times (for bisphenol A) higher degradation kinetics. Fluid dynamics simulation suggested that the flow-through mode greatly enhanced the microscale velocity magnitude and the mass transfer of reactants. Thus, this work presents an ideal platform for the design of 3-D microfluidic-enhanced system for photoelectrochemical applications.

## 1. Introduction

Photoactive electrodes are attracting extensive interests, due to their great potential for addressing the increasing global concerns of environmental remediation and energy production [1–5]. Unfortunately, the practical applicability of this technique is seriously limited by its low energy conversion efficiency. Although much efforts have been devoted to developing new photocatalysts and revealing novel charge separation principles [6–10], most planar photoelectrochemical devices reported suffer from poor interfacial mass transfer and sluggish reaction kinetics [11–14]. 3-D electrodes possess flow-through architecture and large surface areas, therefore can effectively accelerate the charge/reactant diffusion and address the insuperable drawbacks of traditional planar photoanodes, such as low catalyst loading, insufficient reactive sites and poor interfacial contact between catalysts and reactants [15–18]. Consequently, it is worthwhile to explore 3-D photoanodes for photoelectrochemical applications.

To construct high-performance 3-D photoelectrochemical system, one not only needs to exploit unique micro-channels for the fast

transportation of active materials, but also design energetically favorable interface for the fast electron transfer, especially at low potential [15]. From this aspect, there are several prerequisite factors need to be deliberated. Firstly, photoactive semiconductor should possess desirable nanostructures for the fast transportation of charge carriers [19,20]. Secondly, efficient heterostructured interface needs to be explored for the separation of charge carriers [21,22]. However, there is a persistent obstacle caused by depletion region formed at the semiconductor/water interface. For the good electron mobility, the demand of high doping level would unavoidably suppress the width of depletion region, which is unfavorable for the separation of photo-induced electrons and holes [23,24]. Although several strategies have been proved to be effective in overcoming this disadvantage, such as nanostructure design, gradient doping and internal electric field modulation, the extraction of electrons at the semiconductor/substrate interface still remains a bottleneck for exerting the great potential of photoanodes in many cases [25,26]. Schottky junction, in which thermionic emission is the predominant manner for charge transfer, is considered to be very important in the field of diode, photodetector and photovoltaic [27,28].

\* Corresponding author.

E-mail address: [liuruiping@rcees.ac.cn](mailto:liuruiping@rcees.ac.cn) (R. Liu).

<https://doi.org/10.1016/j.apcatb.2018.12.009>

Received 28 August 2018; Received in revised form 4 November 2018; Accepted 3 December 2018

Available online 03 December 2018

0926-3373/ © 2018 Published by Elsevier B.V.

With regard to the photocatalyst/conducting substrate interface, however, the Schottky barrier would block the unidirectional transportation of electrons toward counter electrodes and greatly increase the resistance for the extraction of electrons to the external circuit [25,29]. In this regard, the direct transportation of electrons to the conducting substrate based on Schottky-barrier-free junction is of great importance for the construction of high-performance photoelectrochemical systems.

With this in mind, we report a new design principle of microfluidic-enhanced photoanodes without Schottky barrier for charge transportation. The core concept is to synergize the 3-D high-conductivity carbon substrate with polarization-induced internal electrostatic field, which could provide 1-D channels for direct electron migration. Aligned wurtzite ZnO nanorod arrays, with spontaneous polarization occurring along the *c*-axis ( $0.047 \text{ C m}^{-2}$ ), are used to demonstrate the above hypothesis [30,31]. The 3-D porous structure of flexible carbon cloth not only offers the Schottky-barrier-free interface for electron transfer, but also contributes to the highly efficient mass transportation of reactants. As a result, the 3-D flexible photoelectrochemical cell exhibits significantly improved reaction kinetics than conventional planer photoelectrochemical system at low potential, demonstrating its great potential for environmental and energy applications.

## 2. Methods

### 2.1. Materials

Carbon cloth (WOS 1009) was purchased from Taiwan CeTech Co., Ltd. Zinc acetate dihydrate ( $\text{Zn}(\text{CH}_3\text{COO})_2 \cdot 2\text{H}_2\text{O}$ , ACS reagent, 98%) and zinc nitrate hexahydrate ( $\text{Zn}(\text{NO}_3)_2 \cdot 6\text{H}_2\text{O}$ , reagent grade, 98%) were purchased from Sigma-Aldrich. Dopamine hydrochloride (99%) was obtained from Alfa Aesar. Nitric acid ( $\text{HNO}_3$ , 67%), potassium hydroxide (KOH, 85%), methanol (99.5%), hexamethylenetetramine (HMTA, 99%), sodium sulfate ( $\text{Na}_2\text{SO}_4$ , 99%), silver nitrate ( $\text{AgNO}_3$ , 99.8%), cobalt nitrate hexahydrate ( $\text{Co}(\text{NO}_3)_2 \cdot 6\text{H}_2\text{O}$ , 98.5%) and hydrogen peroxide ( $\text{H}_2\text{O}_2$ , 30%) were purchased from Sinopharm Chemical Reagent Co., Ltd. All reagents are used without further purification.

### 2.2. Preparation of 3-D flow-through photoanodes

Vertically aligned ZnO nanorod arrays were fabricated on carbon cloth following the procedures as illustrated in Scheme 1. To obtain hydrophilic surface, carbon cloth (CC) was treated with nitric acid in a Teflon-lined stainless steel autoclave under  $100^\circ\text{C}$  for 8 h. Bio-inspired polydopamine (PDA) functionalization was carried out to improve the interfacial adhesion between CC and ZnO [32]. In brief, the pretreated carbon cloth was immersed in 10 mM Tris-buffer solution ( $\text{pH} = 8.5$ ) containing  $0.2 \text{ mg mL}^{-1}$  dopamine hydrochloride for 4 h.

A seed-assisted hydrothermal method was used to grow ZnO nanorod arrays onto CC substrates (denoted as CC/ZnO) [33]. Briefly, 6.5 mL KOH solution in methanol (30 mM) was slowly dropped into 12.5 mL methanol containing 10 mM zinc acetate dihydrate at  $60^\circ\text{C}$ . After stirring for 2 h, the PDA coated carbon cloth was immersed in the seed solution for 30 s, which was further annealed at  $200^\circ\text{C}$  for 10 min. The seeding process was repeated several times to obtain a uniform

seed layer. The hydrothermal growth of ZnO nanorod arrays was carried out by dipping the seeded substrate into an aqueous solution of  $\text{Zn}(\text{NO}_3)_2$  (25 mM) and HMTA (25 mM) at  $90^\circ\text{C}$  for 8 h. The same method was used to grow ZnO nanorod arrays onto FTO substrates.

### 2.3. Characterization

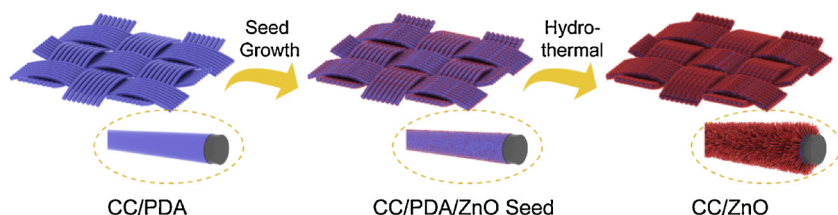
The morphology of samples was characterized by a scanning electron microscope (SEM, JSM-7001F). Transmission electron microscopy (TEM), high-resolution TEM (HR-TEM) and selected area electron diffraction (SAED) were taken on a transmission electron microscope (JEM-2100F) with an acceleration voltage of 200 kV. X-ray photoelectron spectroscopy (XPS) spectra were recorded on a Thermo ESCALAB250Xi spectrometer with a monochromated Al-K $\alpha$  X-ray source. X-ray diffraction (XRD) patterns were recorded on a PANalytical X-ray diffractometer with Cu K $\alpha$  radiation. Raman analysis was carried out on a Renishaw InVia Raman spectrometer with an excitation laser source of 532 nm. The Brunauer-Emmett-Teller (BET) surface area was determined by nitrogen adsorption-desorption isotherm measurements at 77 K (ASAP 2020). The electrical conductivity between ZnO and substrates was measured using a Keithley 2400 multimeter through a two-probe method. The loaded amount of ZnO on the carbon cloth substrate was determined to be  $1.2 \text{ mg cm}^{-2}$  using inductively coupled plasma optical emission spectroscopy (ICP-OES, 710, Agilent Technologies). Electron paramagnetic resonance (EPR) analysis was carried out using a Bruker E500 spectrometer.

### 2.4. Photodeposition of Ag and $\text{Co}_3\text{O}_4$

The photodeposition of Ag and  $\text{Co}_3\text{O}_4$  onto ZnO was carried out using a modified method reported before [34]. ZnO nanorods grown on FTO were scratched and sonicated to prepare a dispersion of ZnO with a concentration of ca.  $0.2 \text{ mg mL}^{-1}$ . In brief, 10 mL ZnO dispersion was mixed with 30 mL distilled water, 5 mL  $\text{AgNO}_3$  aqueous solutions (2 mM) and (or) 5 mL  $\text{Co}(\text{NO}_3)_2$  aqueous solutions (2 mM). The suspension was then irradiated by a 300 W Xe lamp for 10 min under continuous stirring. After centrifuging and washing with water for 3 times, the precipitate was dispersed in ethanol and used for further characterization.

### 2.5. Photoelectrochemical measurements

All the photoelectrochemical measurements were carried out on a Gamry Interface 1000 electrochemical workstation with a three-electrode configuration in 0.1 M  $\text{Na}_2\text{SO}_4$  aqueous solution ( $\text{pH} = 7$ ). A saturated Ag/AgCl electrode and a Pt-wire electrode were used as the reference and counter electrode, respectively. A 500 W Xe lamp (CEL-S500) coupled with an AM 1.5 G filter was used to simulate solar irradiation and the light intensity was calibrated to  $100 \text{ mW cm}^{-2}$ . Photocurrent density vs. voltage (*J*-*V*) curves were measured at a scan rate of  $10 \text{ mV s}^{-1}$ . Before data collection, the *J*-*V* scans were repeated for at least three times to reach a steady state. Electrochemical impedance spectroscopy (EIS) was carried out in the frequency range of  $10^5$  to  $10^{-2} \text{ Hz}$  with an AC voltage amplitude of 10 mV. Scavenger experiments were conducted in the above-mentioned electrolyte containing 0.1 M  $\text{H}_2\text{O}_2$ .



**Scheme 1.** Schematic illustration of the preparation of CC/ZnO composites.

For the pollutant degradation experiments, the as-synthesized photoanode (illuminated area about  $6\text{ cm}^2$ ) was immersed in 20 mL electrolyte containing  $5\text{ mg L}^{-1}$  Rhodamine B (RhB) or bisphenol A (BPA). Control experiment was conducted by adding the same amount of ZnO nanorod powders ( $7.2\text{ mg}$ ) to the above aqueous solution. Magnetic stirring was used to provide a driving force for the contaminated water to flow through the interspace of CC/ZnO electrode. Before irradiation, the suspension solution was stirred in the dark for 1 h to achieve adsorption/desorption equilibrium. After certain time intervals, 1 mL solution was sampled and filtrated to remove particles. The concentration of RhB was detected by UV–vis spectrophotometer (Hitachi UV-3100) at 554 nm. Residual concentration of BPA was determined via an Agilent high performance liquid chromatography (HPLC) system with a C18 column. For BPA, the mobile phase was the mixture of methanol and ultrapure water with a volume ratio of 70:30.

### 2.6. Computational fluid dynamics (CFD) study

The flow fields in the micro-channels were simulated using COMSOL Multiphysics 5.2. The 3-D geometry “CFD” module was used to solve the flow velocity distribution in the electrodes. For the CC/ZnO electrode, two parallel carbon fibers in the same diameter of  $8\text{ }\mu\text{m}$  were separated by a distance of  $4\text{ }\mu\text{m}$ . ZnO nanorods with diameter of  $200\text{ nm}$  and length of  $2\text{ }\mu\text{m}$  were vertically aligned on the surface of both carbon fibers and FTO, with loading densities of about 4 rods per  $\mu\text{m}^2$ . The water flow direction in the CC/ZnO system was set to be perpendicular to the plane of carbon fibers, with an inlet velocity of  $1\text{ mm s}^{-1}$ . For the FTO/ZnO system, water flow direction was parallel to the substrate plane and the inlet velocity was also set to be  $1\text{ mm s}^{-1}$ .

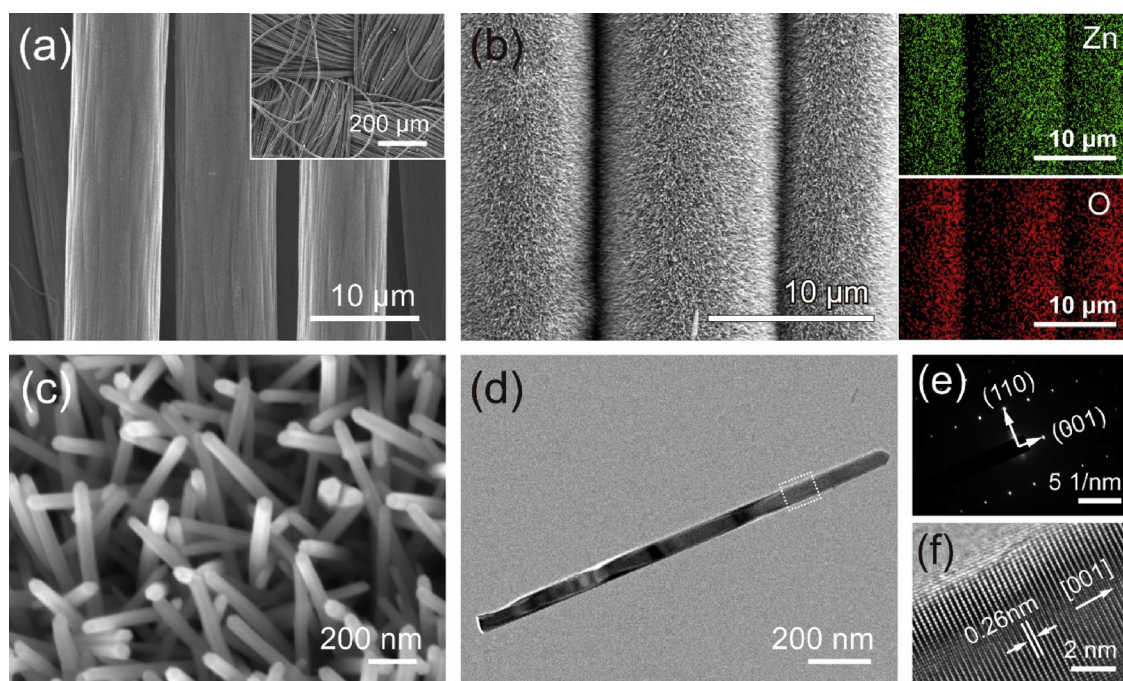
## 3. Results

Fig. 1a shows the texture structure of carbon cloth, woven by carbon fibers with the diameter of ca.  $8\text{ }\mu\text{m}$ . There are many pores among and inside these intertwined carbon fiber bunches. After hydrothermal reaction, one can find that the surface of carbon fibers is uniformly and densely enwrapped by aligned nanorod arrays, forming 3-D

hierarchical structure with sufficient reactive areas (Fig. 1b). Further observation indicates that the typical diameter and length of ZnO nanorods are  $80\text{ nm}$  and  $2\text{ }\mu\text{m}$ , respectively (Fig. 1c and d). The selected area electron diffraction (SAED) pattern in Fig. 1e suggests that ZnO nanorod is grown along the [001] direction with high crystallinity. Meanwhile, the well-resolved lattice spacing of  $0.26\text{ nm}$  in the HR-TEM image corresponds to (001) plane of wurtzite ZnO (Fig. 1f) [35,36]. The excellent flexibility of this CC/ZnO electrode makes it favorable for further flexible device fabrication (Fig. S1).

The detailed structure of CC/ZnO composite was investigated. In Fig. 2a, the XRD peaks at  $26^\circ$  and  $43.2^\circ$  can be assigned to the (002) and (004) planes of graphitic carbon [37]. The other distinctive diffraction peaks can be well indexed to hexagonal wurtzite ZnO (JCPDS 36–1451). The crystal structure is further confirmed by the typical ZnO peaks at  $330$ ,  $437$  and  $1146\text{ cm}^{-1}$  in the Raman spectra (Fig. 2b) [32]. Due to the dense coverage of CC surface by ZnO nanorods, the D- ( $1350\text{ cm}^{-1}$ ) and G-band ( $1590\text{ cm}^{-1}$ ) of pristine CC become weak in the CC/ZnO composites. The formation of CC/ZnO hierarchical architectures is also validated by the XPS analysis. The appearance of strong Zn 2p XPS signals at the binding energy of  $1021\text{ eV}$  and  $1044\text{ eV}$  indicates the successful assembly of ZnO onto CC substrates (Fig. S2). The BET surface area of CC/ZnO is determined to be  $5.43\text{ m}^2\text{ g}^{-1}$  and much higher than that of bare CC ( $1.77\text{ m}^2\text{ g}^{-1}$ ), as shown in Fig. S3. Therefore, a large amount of adsorption and reaction sites can be provided by CC/ZnO for the oxidation reactions.

For 1-D ZnO nanostructures, dipole-moment-induced polarization phenomenon has been revealed by both theoretical and experimental studies [38,39]. As a consequence, the internal electrostatic field exhibits significant impact on the transportation of photo-generated electrons and holes [31]. To study this charge separation behavior, a photodeposition method was carried out (Fig. S4). After the photo-reduction procedure, the formation of Ag nanoparticles on the ends of ZnO nanorods indicates the end-accumulation of photogenerated electrons in anisotropic ZnO nanorods. In contrast, the growth of  $\text{Co}_3\text{O}_4$  nanoparticles on the lateral facets suggests the different spatial distribution of hole-mediated oxidation sites. This selective deposition of Ag and  $\text{Co}_3\text{O}_4$  well evidences the internal electrostatic field-induced



**Fig. 1.** SEM images of CC (a) and CC/ZnO (b and c). The inset image in panel a shows the texture structure of CC. The energy dispersive spectroscopy (EDS) mapping images of CC/ZnO are also shown in panel b. (d) TEM image of a single ZnO nanorod. The SAED pattern (e) and HR-TEM image (f) correspond to the circled region in panel d.



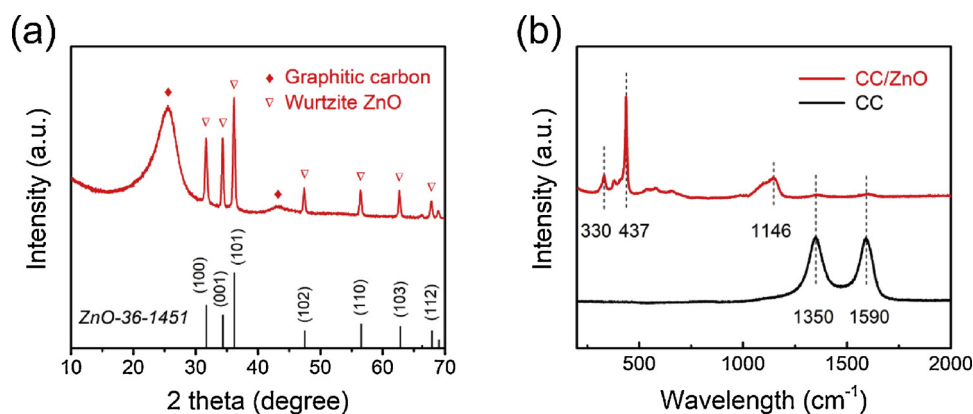


Fig. 2. XRD patterns (a) and Raman spectra (b) of CC/ZnO composites.

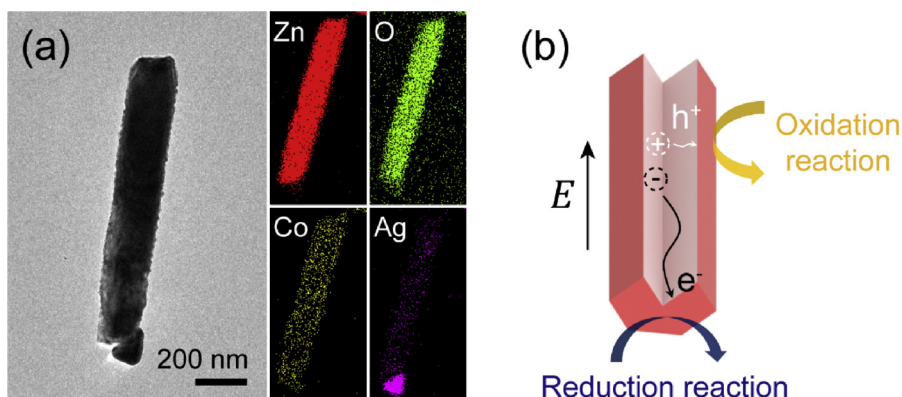


Fig. 3. (a) TEM image and the corresponding element mapping of Ag and  $\text{Co}_3\text{O}_4$  deposited ZnO, which was fabricated by photodeposition method. (b) Schematic of the spatial separation of electron-hole pairs in the presence of internal electric field.

separation of electrons and holes (Fig. 3a). The element mapping images further confirm the different distribution of Co and Ag on the surface of ZnO nanorod. Based on the above results, we can deduce that electron transportation along the axial direction is greatly facilitated by internal electric field, while holes with relatively low mobility would migrate to the side surface of ZnO (Fig. 3b). The spatial separation of electron-hole pairs in anisotropic ZnO provides ideal photoactive semiconductor for the construction of Schottky-barrier-free photoelectrochemical system.

With electrons accumulated on the end of ZnO nanorods, the interfacial contact between ZnO and conducting substrate is of substantial importance for the efficient extraction of electrons to the external circuit. Therefore, the electrical contact between ZnO and graphitic

carbon was investigated by a two-probe method, as illustrated in Fig. 4a. The current-voltage (I–V) behaviors of ZnO grown on commercial FTO glass and graphite substrates are shown in Fig. 4b. Non-linear I–V characteristics, similar to the rectification behavior in diodes, is clearly observed for FTO/ZnO stack [29]. Interestingly, graphite/ZnO exhibits a typical ohmic behavior, indicating the elimination of interfacial Schottky barrier. In principle, the facilitated migration of spontaneously separated electrons across the heterostructured interface could significantly contribute to the activity of photoelectrodes.

Having realized the interfacial separation of photogenerated charge carriers, the impact of 3-D structure on the mass transfer of reactant molecules at photoanodes was deliberated. CFD simulation was carried out to visualize the velocity field at the surface of ZnO nanorods. The

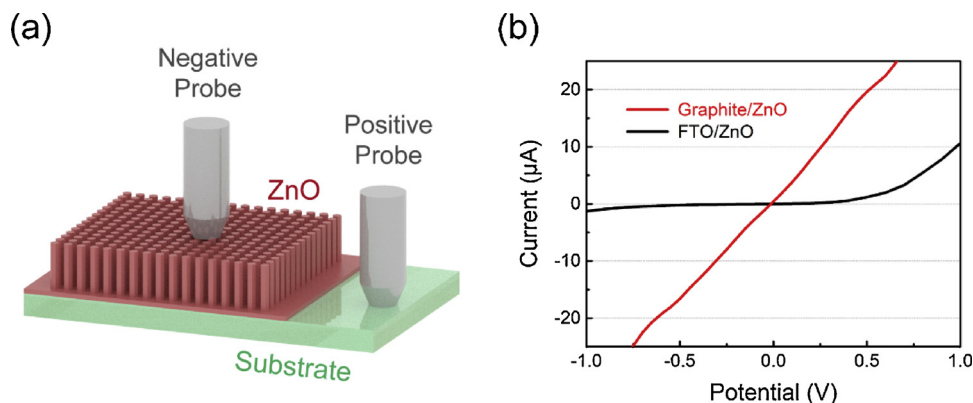
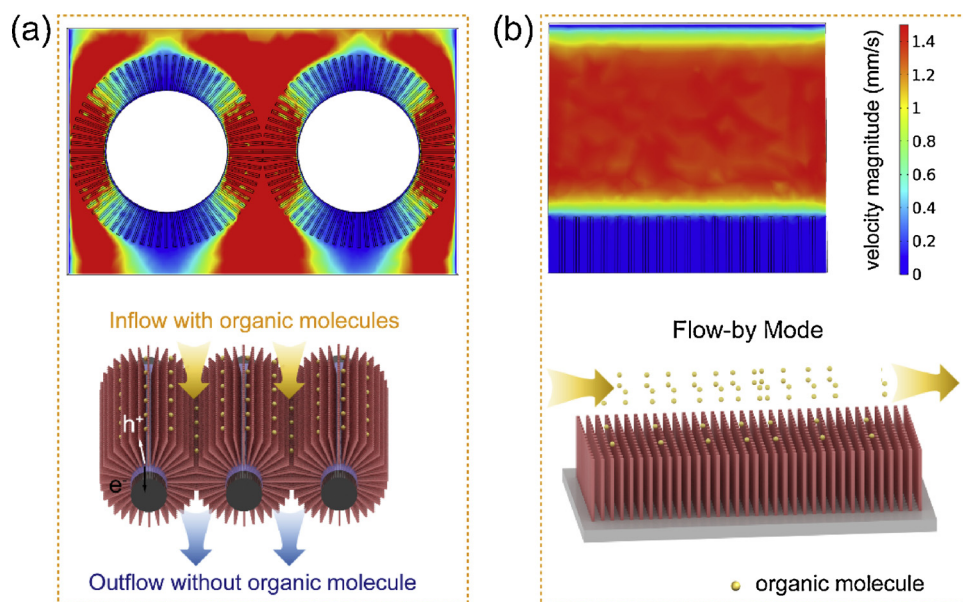


Fig. 4. (a) Schematic illustration of two-probe device used to measure the interfacial electrical conductivity. (b) Current-voltage (I–V) curves of two typical ZnO-based composite electrodes.



**Fig. 5.** CFD simulations of the flow behaviors in the flow-through and flow-by electrodes. (a) The flow field distribution (up) and schematic illustration (bottom) of CC/ZnO flow-through electrode. (b) The flow field distribution (up) and schematic illustration (bottom) of FTO/ZnO. The velocity magnitude contours in panel a share the same color scale with that in panel b.

velocity magnitude contours of the 3-D flow-through electrodes are shown in Fig. 5a. It can be observed that the flow-through mode leads to a fast microfluidic flow in the interspace of CC/ZnO. This distribution of flow field enables the rapid diffusion of organic matters. Thus, the 3-D hierarchical nanostructure offers ideal photoactive surface for microfluidic-enhanced pollutant degradation. In contrast, the flow-by mode in FTO/ZnO only favors the lateral flow of water on the surface of bulk electrode, with no liquid flowing into the interspace of ZnO nanorods (Fig. 5b). Under this circumstance, the diffusion of reactants towards the reactive sites on ZnO mainly depends on their concentration gradients. The difficulty in mass transfer unavoidably causes the poor degradation efficiency of planar photoanodes.

With improved charge separation and enhanced mass transfer, the photoelectrochemical performance of CC/ZnO photoanodes was evaluated using a three-electrode electrochemical system. In comparison to FTO/ZnO photoanode, CC/ZnO presents more negative open circuit potential, implying the smaller photovoltage loss across the heterostructured interface (Fig. S5). Fig. 6a shows the current density versus applied potential (*J*-*V*) curves of different ZnO electrodes recorded in the dark and under irradiation. As expected, a high photocurrent density of  $1 \text{ mA}\cdot\text{cm}^{-2}$  at 1.23 V vs. RHE is achieved for ZnO nanorods grown on carbon cloth, which is superior to those on FTO substrate. Amazingly, the photocurrent of CC/ZnO increases rapidly with the increase of applied bias and hits a plateau at only 0.5 V vs. RHE. This value is much lower than that (0.9 V vs. RHE) of FTO/ZnO photoanode.

Accordingly, there is a significant increase in the applied bias photon-to-current efficiency (ABPE) for CC/ZnO, as shown in Fig. S6. Considering that excessively positive onset potential is one of the limiting factors for the exploration of high-performance photoanodes, surface cocatalysts such as  $\text{RuO}_2$ ,  $\text{IrO}_2$  and Co-based compounds are usually used to accelerate the oxidation kinetics [13,14]. Our results demonstrate that the strategically integration of internal electric field with 3-D carbon substrate can effectively improve the charge transfer kinetics and decrease the onset potential of electrodes. This can be well demonstrated by the 4 times higher photocurrent of CC/ZnO than FTO/ZnO photoanodes at 0.5 V vs. RHE (Fig. 6b). Moreover, the coating of PDA layer exerts a positive influence on the long-term stability of CC/ZnO, with no impact on its initial photoresponse (Fig. S7). Thus, we provide a new opportunity to construct high-performance photoelectrochemical devices with free energy barrier and low energy consumption. Furthermore, extraordinary PEC performance can be also achieved in other carbon/ZnO systems, such as carbon paper/ZnO and graphite/ZnO electrodes (Fig. S8). The high efficiency and adaptability of carbon/ZnO photoanodes offer great opportunities for their promising applications in solar energy conversion.

Employing carbon cloth with multi-channels as substrate, the potential of 3-D CC/ZnO photoanode for organic pollutant degradation was thereafter evaluated. As illustrated in Fig. 7a, contaminated water can flow through the interspace of 3-D CC/ZnO electrode, enabling the maximum utilization of surface reactive sites, i.e. the enhanced rates of

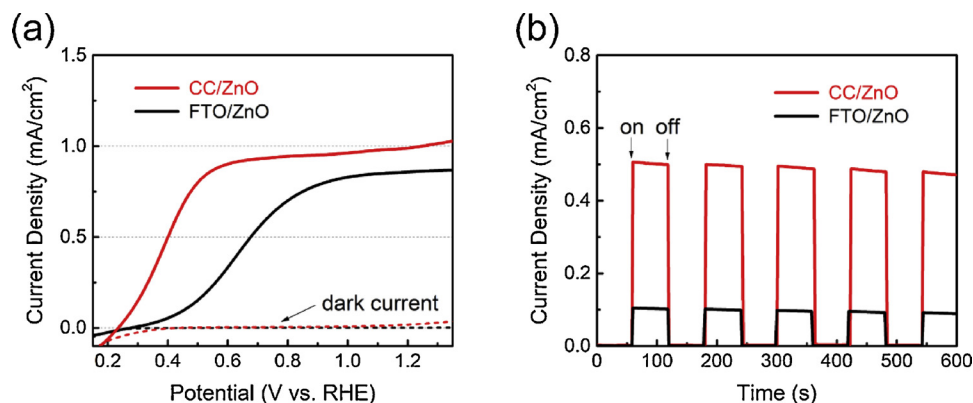


**Fig. 6.** (a) *J*-*V* curves of CC/ZnO and FTO/ZnO photoanodes. Solid and dashed lines represent light and dark conditions, respectively. (b) Long-term photocurrent measurements of CC/ZnO and FTO/ZnO photoanodes at 0.5 V vs. RHE.

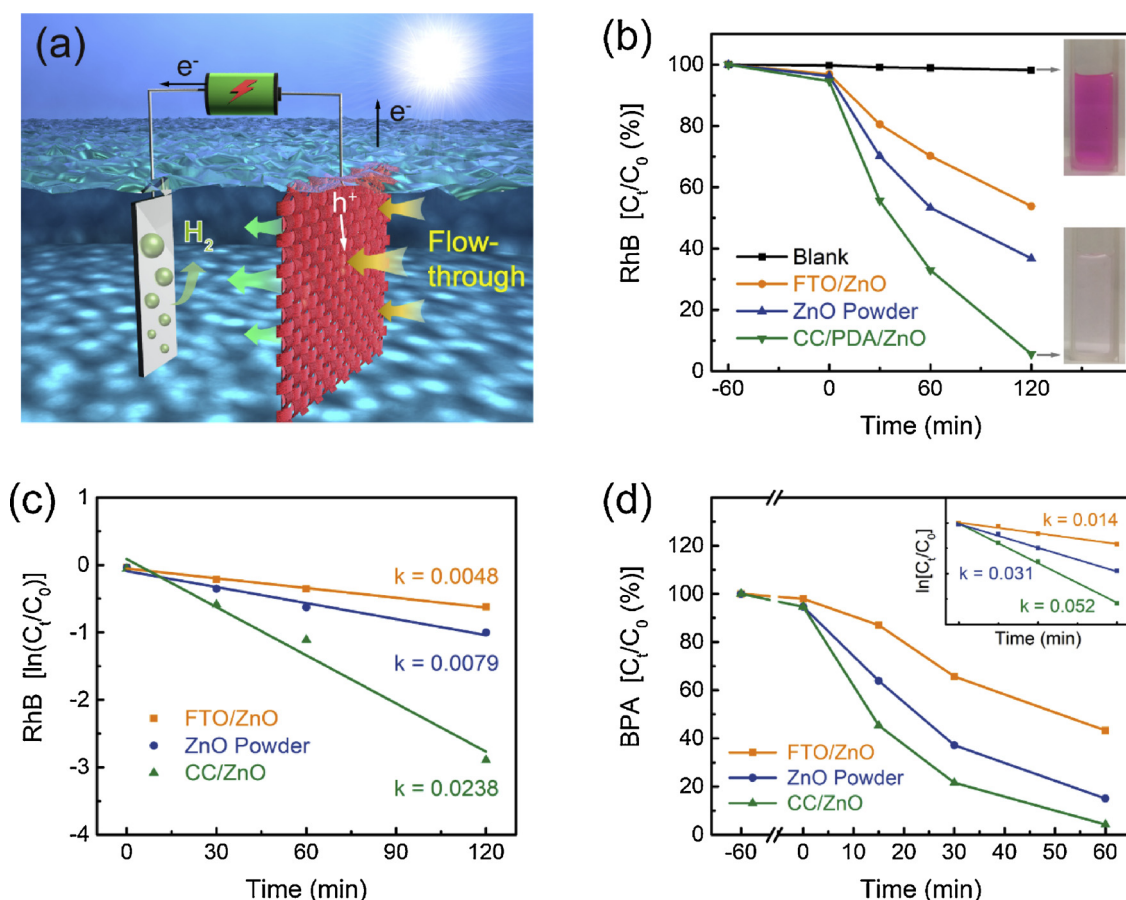


**Fig. 7.** (a) Schematic illustration of 3D flow-through photoanode based on CC/ZnO nanostructures. (b) Degradation rates of RhB as a function of irradiation time in different photodegradation systems. The current density of photoanodes are set to be  $0.1 \text{ mA cm}^{-2}$ . Insets show the images of RhB solutions before and after photocatalytic reaction. (c) Kinetics simulation curves of RhB in different systems. (d) Degradation rates and the corresponding kinetics plots of BPA in different systems.

mass transportation [16,17]. For the photocatalytic degradation of toxic dyes, CC/ZnO photoanode presents the best photocatalytic activity and more than 95% of Rhodamine B (RhB) is decomposed within 120 min (Fig. 7b). However, only 45% and 62% of RhB are degraded over FTO/ZnO photoanode and suspended ZnO nanorods under the same condition. In general, either zero-order or pseudo-first-order kinetics can be used to simulate the photocatalytic reaction [40–43]. Based on repeated verification (Fig. S9), it seems that the latter model fits our degradation results much better. Therefore, pseudo-first-order kinetics is employed to simulate all the photocatalytic degradation plots, as shown in Fig. 7c. CC/ZnO with a flow-through mode shows a rate constant of  $0.0238 \text{ min}^{-1}$ , which is 4 times higher than FTO/ZnO and 2 times higher than suspended ZnO nanorods. Furthermore, there is negligible decrease of activity after five cycling runs, indicating the excellent photostability of CC/ZnO photoanodes (Fig. S9). Bisphenol A (BPA), a representative environmental contaminant that is responsible for reproductive damages to aquatic organisms, was also used to evaluate the photoelectrochemical performance of microfluidic-enhanced photoanodes. As shown in Fig. 7d, 3-D CC/ZnO photoanode displays 270% and 70% higher degradation kinetics ( $k = 0.052 \text{ min}^{-1}$ ) than that of planar FTO/ZnO photoanode ( $k = 0.014 \text{ min}^{-1}$ ) and ZnO powder ( $k = 0.031 \text{ min}^{-1}$ ), respectively, verifying the feasibility of flow-through photoelectro-reactor for efficient pollutant removal. What's more, this idea of flow-through photoanode can be applied to many other semiconductors (e.g.,  $\text{WO}_3$  and  $\text{TiO}_2$ ), showing its broad and potential application prospect (Fig. S10).

The interfacial behavior of charge carriers was investigated to find out the fundamental reasons for the excellent photoelectrochemical

performance of CC/ZnO photoanodes. According to previous reports, the work functions of both CC and FTO are around 5.0 eV, while the Fermi level of ZnO is about 4.2 eV [15,29]. Generally speaking, Schottky barrier will form across both the CC/ZnO and FTO/ZnO interface because of the higher work function of substrate than the Fermi level of semiconductor. Based on the contact theory, a thermionic emission mechanism can be used to illustrate the interfacial charge transfer in the FTO/ZnO system [25]. As shown in Fig. 8a, electrons have to overcome the interfacial potential barrier to reach the substrate. This inevitably leads to an increased voltage loss and decreased photocurrent output. On the contrary, electron tunneling seems to be the dominant mechanism for the charge transfer through the CC/ZnO interface. As depicted in Fig. 8b, electrons take an energetically favorable pathway to reach the substrate, which facilitates the charge transportation as well as charge diffusion coefficient. Considering that crystal defects (mainly oxygen vacancies) might contribute to the improved electron transfer and consequently the photoresponse, EPR measurements of ZnO grown on CC and FTO were conducted. The resulting EPR spectra indicate that growth substrate has negligible influence on the defects of ZnO (Fig. S11) [10]. Meanwhile, annealing treatment of the electrodes in air was carried out at  $450^\circ\text{C}$  for 2 h to acquire defect-free samples. The obtained photoanodes show comparable photocurrent densities to the pristine ones, excluding the possible contribution of defects in ZnO to the enhanced photoresponse (Fig. S12). Note that strong EPR signal corresponding to carbon defects is observed at  $g = 2.00$  for CC substrates (Fig. S11), it is reasonably believed that strong interfacial interactions between ZnO and CC substrates contribute to the fast electron transfer [44].

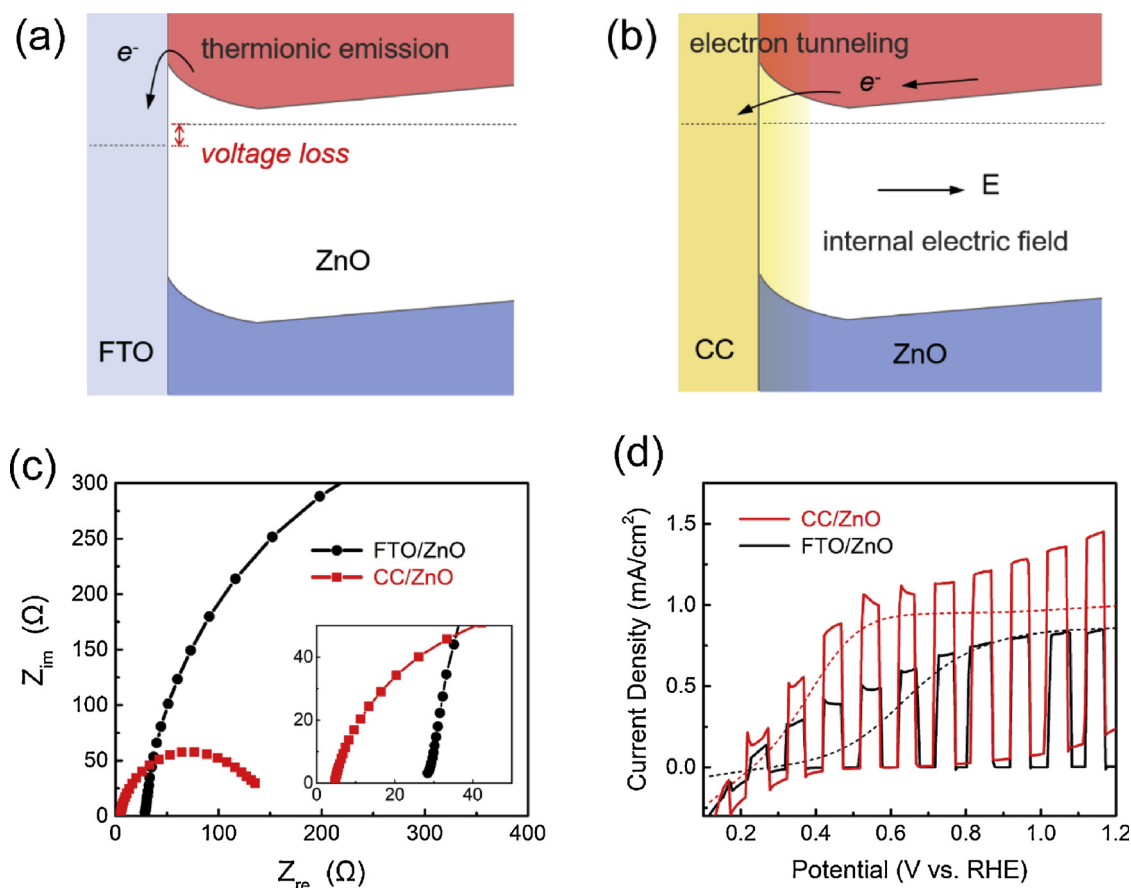


**Fig. 8.** Schematic illustration showing the energy band position and interfacial electron transfer mechanisms of FTO/ZnO (a) and CC/ZnO (b) interface. The presence of internal electrostatic field is also displayed. (c) Nyquist plots of CC/ZnO and FTO/ZnO recorded at 0.5 V vs. RHE. (d) J–V curves of CC/ZnO and FTO/ZnO photoanodes with (solid lines) and without (dashed lines)  $\text{H}_2\text{O}_2$ .

To support this deduction, EIS measurements were carried out on these two kinds of photoanodes. In comparison with FTO/ZnO, a remarkably decreased arc radius is observed in the Nyquist plot of CC/ZnO, demonstrating its low charge transfer resistance (Fig. 8c). Enlarged Nyquist plots in the inset of Fig. 8c further confirms the lower series resistance of CC/ZnO (5  $\Omega$ ) than that of FTO/ZnO (30  $\Omega$ ). This suggests the improved conductivity of 3-D CC/ZnO photoanodes, which is consistent with the above results. As shown in Figs. 3 and 8b, internal electrostatic field in anisotropic ZnO offers extra driving force for the migration of electrons to the end of ZnO nanorod. This effect facilitates the bulk separation of photo-induced charge carriers. On the other hand, graphitic carbon cloth (CC) substrate provides a barrier-free interface for the fast transfer of electrons from ZnO to CC, as evidenced by the current-voltage (I–V) measurements. Consequently, synergetic interactions between ZnO and CC results in the significantly improved charge separation both in the bulk and around heterostructured interface of photoanodes. Meanwhile, abundant holes are accumulated at the lateral surface of ZnO nanorods, providing more reactive sites for photooxidation reactions. To validate the superior charge separation ability of 3-D hierarchical photoanode, scavenging experiments were conducted by employing  $\text{H}_2\text{O}_2$  as hole scavenger. As shown in Fig. 8d, the addition of  $\text{H}_2\text{O}_2$  only exhibits slight influence on the photocurrent density of CC/ZnO, indicating the nearly 100% utilization of photo-carriers over the full range of voltages. In comparison, there is an obvious increase of photoresponse of FTO/ZnO after the addition of  $\text{H}_2\text{O}_2$ , especially at low bias potential. All these results suggest that the barrier-free interface between anisotropic ZnO and carbon cloth can greatly contribute to the superior photoactivity of CC/ZnO photoanode [31].

#### 4. Conclusion

In this work, we report the construction of 3-D CC/ZnO heterostructures as microfluidic-enhanced photoanodes for photoelectrochemical applications. Through integrating the internal electric field in anisotropic ZnO and the ohmic interface between ZnO and carbon substrate, photogenerated charge carriers are efficiently separated. This enhancement of interfacial charge transportation leads to significantly increased photocurrent at low bias potential. More importantly, the hierarchical architecture of CC/ZnO provides microfluidic channels for the efficient mass transportation. Benefiting from the flow-through structure and barrier-free interface, the as-synthesized microfluidic-enhanced photoanodes exhibit much superior photoactivity than planar FTO/ZnO photoanodes for Rhodamine B and bisphenol A degradation. This work provides new pathway for the design of flexible microfluidic-enhanced devices for photoelectrochemical applications, such as environment remediation, solar fuel production and flexible electronics.

#### Acknowledgements

This work was supported by the National Natural Science Foundation of China (grant nos. 51538013, 51578531, 51722811). This work was also supported by the National Key R&D Program of China (Grant no. 2016YFC0400502).

#### Appendix A. Supplementary data

Supplementary material related to this article can be found, in the online version, at doi:<https://doi.org/10.1016/j.apcatb.2018.12.009>.



## References

- [1] L. Wu, F. Li, Y. Xu, J.W. Zhang, D. Zhang, G. Li, H. Li, Plasmon-induced photoelectrocatalytic activity of Au nanoparticles enhanced TiO<sub>2</sub> nanotube arrays electrodes for environmental remediation, *Appl. Catal. B Environ.* 164 (2015) 217–224, <https://doi.org/10.1016/j.apcatb.2014.09.029>.
- [2] G. Li, Z. Lian, W. Wang, D. Zhang, H. Li, Nanotube-confinement induced size-controllable g-C<sub>3</sub>N<sub>4</sub> quantum dots modified single-crystalline TiO<sub>2</sub> nanotube arrays for stable synergetic photoelectrocatalysis, *Nano Energy* 19 (2016) 446–454, <https://doi.org/10.1016/j.nanoen.2015.10.011>.
- [3] X. An, T. Li, B. Wen, J. Tang, Z. Hu, L.-M. Liu, J. Qu, C.P. Huang, H. Liu, New insights into defect-mediated heterostructures for photoelectrochemical water splitting, *Adv. Energy Mater.* (2016) 1502268, <https://doi.org/10.1002/aenm.201502268>.
- [4] X. An, L. Zhang, B. Wen, Z. Gu, L.-M. Liu, J. Qu, H. Liu, Boosting photoelectrochemical activities of heterostructured photoanodes through interfacial modulation of oxygen vacancies, *Nano Energy* 35 (2017) 290–298, <https://doi.org/10.1016/j.nanoen.2017.04.002>.
- [5] Z. Gu, L. Zhang, B. Wen, X. An, H. Lan, L.-M. Liu, T. Chen, J. Zhang, X. Cao, J. Tang, H. Liu, J. Qu, Efficient design principle for interfacial charge separation in hydrogen-intercalated nonstoichiometric oxides, *Nano Energy* 53 (2018) 887–897, <https://doi.org/10.1016/j.nanoen.2018.09.019>.
- [6] S. Xiao, P. Liu, W. Zhu, G. Li, D. Zhang, H. Li, Copper nanowires: a substitute for noble metals to enhance photocatalytic H<sub>2</sub> generation, *Nano Lett.* 15 (2015) 4853–4858, <https://doi.org/10.1021/acs.nanolett.5b00082>.
- [7] S. Wang, S. Lin, D. Zhang, G. Li, M.K.H. Leung, Controlling charge transfer in quantum-size titania for photocatalytic applications, *Appl. Catal. B Environ.* 215 (2017) 85–92, <https://doi.org/10.1016/j.apcatb.2017.05.043>.
- [8] D. Pan, Z. Han, Y. Miao, D. Zhang, G. Li, Thermally stable TiO<sub>2</sub> quantum dots embedded in SiO<sub>2</sub> foams: characterization and photocatalytic H<sub>2</sub> evolution activity, *Appl. Catal. B Environ.* 229 (2018) 130–138, <https://doi.org/10.1016/j.apcatb.2018.02.022>.
- [9] X. Wang, X. Zhao, D. Zhang, G. Li, H. Li, Microwave irradiation induced UiO-66-NH<sub>2</sub> anchored on graphene with high activity for photocatalytic reduction of CO<sub>2</sub>, *Appl. Catal. B Environ.* 228 (2018) 47–53, <https://doi.org/10.1016/j.apcatb.2018.01.066>.
- [10] T. Wei, Y.-N. Zhu, Z. Gu, X. An, L.-m. Liu, Y. Wu, H. Liu, J. Tang, J. Qu, Multi-electric field modulation for photocatalytic oxygen evolution: enhanced charge separation by coupling oxygen vacancies with faceted heterostructures, *Nano Energy* 51 (2018) 764–773, <https://doi.org/10.1016/j.nanoen.2018.07.018>.
- [11] J.-M. Wu, Y. Chen, L. Pan, P. Wang, Y. Cui, D. Kong, L. Wang, X. Zhang, J.-J. Zou, Multi-layer monoclinic BiVO<sub>4</sub> with oxygen vacancies and V<sup>4+</sup> species for highly efficient visible-light photoelectrochemical applications, *Appl. Catal. B Environ.* 221 (2018) 187–195, <https://doi.org/10.1016/j.apcatb.2017.09.031>.
- [12] L. Li, X. Zhao, D. Pan, G. Li, Nanotube array-like WO<sub>3</sub>/W photoanode fabricated by electrochemical anodization for photoelectrocatalytic overall water splitting, *Chin. J. Catal.* 38 (2017) 2132–2140, [https://doi.org/10.1016/S1872-2067\(17\)62948-6](https://doi.org/10.1016/S1872-2067(17)62948-6).
- [13] Q.H. Liu, J.F. He, T. Yao, Z.H. Sun, W.R. Cheng, S. He, Y. Xie, Y.H. Peng, H. Cheng, Y.F. Sun, Y. Jiang, F.C. Hu, Z. Xie, W.S. Yan, Z.Y. Pan, Z.Y. Wu, S.Q. Wei, Aligned Fe<sub>2</sub>TiO<sub>5</sub>-containing nanotube arrays with low onset potential for visible-light water oxidation, *Nat. Commun.* 5 (2014) 5122, <https://doi.org/10.1038/ncomms6122>.
- [14] D. Cao, W. Luo, J. Feng, X. Zhao, Z. Li, Z. Zou, Cathodic shift of onset potential for water oxidation on a Ti<sup>4+</sup>-doped Fe<sub>2</sub>O<sub>3</sub> photoanode by suppressing the back reaction, *Energy Environ. Sci.* 7 (2014) 752–759, <https://doi.org/10.1039/C3EE42722F>.
- [15] X.Y. Xu, G. Zhou, X.F. Dong, J.G. Hu, Interface band engineering charge transfer for 3D MoS<sub>2</sub> photoanode to boost photoelectrochemical water splitting, *ACS Sustain. Chem. Eng.* 5 (2017) 3829–3836, <https://doi.org/10.1021/acsschemeng.6b02883>.
- [16] Q.H. Ji, D.W. Yu, G. Zhang, H.C. Lan, H.J. Liu, J.H. Qu, Microfluidic flow through polyaniline supported by lamellar-structured graphene for mass-transfer-enhanced electrocatalytic reduction of hexavalent chromium, *Environ. Sci. Technol.* 49 (2015) 13534–13541, <https://doi.org/10.1021/acs.est.5b03314>.
- [17] Y. Zhou, Q. Ji, H. Liu, J. Qu, Pore structure-dependent mass transport in flow-through electrodes for water remediation, *Environ. Sci. Technol.* (2018), <https://doi.org/10.1021/acs.est.8b01728>.
- [18] X.J. Men, H.B. Chen, K.W. Chang, X.F. Fang, C.F. Wu, W.P. Qin, S.Y. Yin, Three-dimensional free-standing ZnO/graphene composite foam for photocurrent generation and photocatalytic activity, *Appl. Catal. B Environ.* 187 (2016) 367–374, <https://doi.org/10.1016/j.apcatb.2016.01.052>.
- [19] H. Lan, L. Li, X. An, F. Liu, C. Chen, H. Liu, J. Qu, Microstructure of carbon nitride affecting synergetic photocatalytic activity: hydrogen bonds vs. structural defects, *Appl. Catal. B Environ.* 204 (2017) 49–57, <https://doi.org/10.1016/j.apcatb.2016.11.022>.
- [20] X. Chen, H. Zhang, D. Zhang, Y. Miao, G. Li, Controllable synthesis of mesoporous multi-shelled ZnO microspheres as efficient photocatalysts for NO oxidation, *Appl. Surf. Sci.* 435 (2018) 468–475, <https://doi.org/10.1016/j.apsusc.2017.11.045>.
- [21] X. An, C. Hu, H. Liu, J. Qu, Oxygen vacancy mediated construction of anatase/brookite heterophase junctions for high-efficiency photocatalytic hydrogen evolution, *J. Mater. Chem. A Mater. Energy Sustain.* 5 (2017) 24989–24994, <https://doi.org/10.1039/C7TA08809D>.
- [22] X. An, C. Hu, H. Lan, H. Liu, J. Qu, strongly coupled metal oxide/reassembled carbon nitride/Co-Pi heterostructures for efficient photoelectrochemical water splitting, *ACS Appl. Mater. Interfaces* 10 (2018) 6424–6432, <https://doi.org/10.1021/acsami.8b01070>.
- [23] M.Z. Liu, J.L. Lyons, D.H. Yan, M.S. Hybertsen, Semiconductor-based photoelectrochemical water splitting at the limit of very wide depletion region, *Adv. Funct. Mater.* 26 (2016) 219–225, <https://doi.org/10.1002/adfm.201503692>.
- [24] M.R. Morris, S.R. Pendlebury, J. Hong, S. Dunn, J.R. Durrant, Effect of internal electric fields on charge carrier dynamics in a ferroelectric material for solar energy conversion, *Adv. Mater.* 28 (2016) 7123–7128, <https://doi.org/10.1002/adma.201601238>.
- [25] J. Chen, L. Zhang, Z. Lam, H.B. Tao, Z. Zeng, H.B. Yang, J. Luo, L. Ma, B. Li, J. Zheng, S. Jia, Z. Wang, Z. Zhu, B. Liu, Tunneling interlayer for efficient transport of charges in metal oxide electrodes, *J. Am. Chem. Soc.* 138 (2016) 3183–3189, <https://doi.org/10.1021/jacs.5b13464>.
- [26] H. Ma, W. Ma, J.-F. Chen, X.-Y. Liu, Y.-Y. Peng, Z.-Y. Yang, H. Tian, Y.-T. Long, Quantifying visible-light-induced electron transfer properties of single dye-sensitized ZnO entity for water splitting, *J. Am. Chem. Soc.* 140 (2018) 5272–5279, <https://doi.org/10.1021/jacs.8b01623>.
- [27] J.D. Jin, J.W. Zhang, A. Shaw, V.N. Kudina, I.Z. Mitrovic, J.S. Wrench, P.R. Chalker, C. Balocco, A.M. Song, S. Hall, A high speed PE-ALD ZnO Schottky diode rectifier with low interface-state density, *J. Phys. D* 51 (2018), <https://doi.org/10.1088/1361-6463/aaa4a2>.
- [28] L.J. Guo, Z. Yang, X.C. Dou, Artificial olfactory system for trace identification of explosive vapors realized by optoelectronic schottky sensing, *Adv. Mater.* 29 (2017), <https://doi.org/10.1002/adma.201604528>.
- [29] E. Edri, N. Kedem, H. Cohen, P. Barnes, G. Hodes, Higher open circuit voltage and reduced UV-Induced reverse current in ZnO-based solar cells by a chemically modified blocking layer, *J. Phys. Chem. C* 118 (2014) 16884–16891, <https://doi.org/10.1021/jp5004209>.
- [30] M. Hellström, I. Beinik, P. Broqvist, J.V. Lauritsen, K. Hermansson, Subsurface hydrogen bonds at the polar Zn-terminated ZnO(0001) surface, *Phys. Rev. B* 94 (2016) 245433, <https://doi.org/10.1103/PhysRevB.94.245433>.
- [31] B. Zhang, Z.Y. Wang, B.B. Huang, X.Y. Zhang, X.Y. Qin, H.L. Li, Y. Dai, Y.J. Li, Anisotropic photoelectrochemical (PEC) performances of ZnO single-crystalline photoanode: effect of internal electrostatic fields on the separation of photo-generated charge carriers during PEC water splitting, *Chem. Mater.* 28 (2016) 6613–6620, <https://doi.org/10.1021/acs.chemmater.6b02639>.
- [32] N. Zheng, Y. Huang, W. Sun, X. Du, H.-Y. Liu, S. Moody, J. Gao, Y.-W. Mai, In-situ pull-off of ZnO nanowire from carbon fiber and improvement of interlaminar toughness of hierarchical ZnO nanowire/carbon fiber hybrid composite laminates, *Carbon* 110 (2016) 69–78, <https://doi.org/10.1016/j.carbon.2016.09.002>.
- [33] T. Lee, W. Lee, S.-W. Kim, J.J. Kim, B.-S. Kim, Flexible textile strain wireless sensor functionalized with hybrid carbon nanomaterials supported ZnO nanowires with controlled aspect ratio, *Adv. Funct. Mater.* 26 (2016) 6206–6214, <https://doi.org/10.1002/adfm.201601237>.
- [34] R. Li, H. Han, F. Zhang, D. Wang, C. Li, Highly efficient photocatalysts constructed by rational assembly of dual-cocatalysts separately on different facets of BiVO<sub>4</sub>, *Energy Environ. Sci.* 7 (2014) 1369–1376, <https://doi.org/10.1039/C3EE43304H>.
- [35] Y.C. Liu, Z. Kang, H.N. Si, P.F. Li, S.Y. Cao, S. Liu, Y. Li, S.C. Zhang, Z. Zhang, Q.L. Liao, L. Wang, Y. Zhang, Cactus-like hierarchical nanorod-nanosheet mixed dimensional photoanode for efficient and stable water splitting, *Nano Energy* 35 (2017) 189–198, <https://doi.org/10.1016/j.nanoen.2017.03.042>.
- [36] S.Y. Cao, X.Q. Yan, Z. Kang, Q.J. Liang, X.Q. Liao, Y. Zhang, Band alignment engineering for improved performance and stability of ZnFe<sub>2</sub>O<sub>4</sub> modified CdS/ZnO nanostructured photoanode for PEC water splitting, *Nano Energy* 24 (2016) 25–31, <https://doi.org/10.1016/j.nanoen.2016.04.001>.
- [37] Y. Zhong, D. Chao, S. Deng, J. Zhan, R. Fang, Y. Xia, Y. Wang, X. Wang, X. Xia, J. Tu, Confining sulfur in integrated composite scaffold with highly porous carbon Fibers/Vanadium nitride arrays for high-performance lithium-sulfur batteries, *Adv. Funct. Mater.* (2018) 1706391, <https://doi.org/10.1002/adfm.201706391>.
- [38] C. Wöll, The chemistry and physics of zinc oxide surfaces, *Prog. Surf. Sci.* 82 (2007) 55–120, <https://doi.org/10.1016/j.progsurf.2006.12.002>.
- [39] Y.-J. Wu, C.-H. Liao, C.-Y. Hsieh, P.-M. Lee, Y.-S. Wei, Y.-S. Liu, C.-H. Chen, C.-Y. Liu, Local electronic structures and polarity of ZnO nanorods grown on GaN substrates, *J. Phys. Chem. C* 119 (2015) 5122–5128, <https://doi.org/10.1021/jp5116542>.
- [40] X. Chen, S.N. Choing, D.J. Aschaffenburg, C.D. Pemmaraju, D. Prendergast, T. Cuk, The formation Time of Ti–O• and Ti–O–Ti radicals at the n-SrTiO<sub>3</sub>/aqueous Interface during photocatalytic water oxidation, *J. Am. Chem. Soc.* (2016), <https://doi.org/10.1021/jacs.6b09550>.
- [41] X. Sheng, Z. Liu, R. Zeng, L. Chen, X. Feng, L. Jiang, Enhanced photocatalytic reaction at air–liquid–solid joint interfaces, *J. Am. Chem. Soc.* 139 (2017) 12402–12405, <https://doi.org/10.1021/jacs.7b07187>.
- [42] G. Zhang, Q. Ji, Z. Wu, G. Wang, H. Liu, J. Qu, J. Li, Facile “Spot-Heating” synthesis of carbon dots/carbon nitride for solar hydrogen evolution synchronously with contaminant decomposition, *Adv. Funct. Mater.* 28 (2018) 1706462, <https://doi.org/10.1002/adfm.201706462>.
- [43] X. Li, S. Liu, D. Cao, R. Mao, X. Zhao, Synergetic activation of H<sub>2</sub>O<sub>2</sub> by photo-generated electrons and cathodic Fenton reaction for enhanced self-driven photoelectrocatalytic degradation of organic pollutants, *Appl. Catal. B Environ.* 235 (2018) 1–8, <https://doi.org/10.1016/j.apcatb.2018.04.042>.
- [44] D. Savchenko, V. Vorlíček, A. Prokhorov, E. Kalabukhova, J. Lančok, M. Jelínek, Raman and EPR spectroscopic studies of chromium-doped diamond-like carbon films, *Diam. Relat. Mater.* 83 (2018) 30–37, <https://doi.org/10.1016/j.diamond.2018.01.021>.